JMEPEG
https://doi.org/10.1007/s11665-022-06603-z

1059-9495/$19.00

TECHNICAL ARTICLE

Microstructure-Based MultiStage Fatigue Modeling of NiTi Alloy Fabricated via Direct Energy Deposition (DED)

Allen Bagheri, Aref Yadollahi, Mohammad J. Mahtabi, Yubraj Paudel, Ethan Vance, Nima Shamsaei, and Mark F. Horstemeyer

Submitted: 23 September 2021 / Accepted: 17 December 2021

A microstructure-based multistage fatigue (MSF) model was employed to study the process–structure–property relations for cyclic damage and fatigue life of NiTi alloy fabricated via an additive manufacturing (AM) technique. Various defect characteristics (*i.e.,* level of porosity, pore size, and their spacing) and microstructural features (*i.e.,* grain size, mean grain orientation, and misorientation angles), dictated by the manufacturing and post-manufacturing heat treatment processes, were used to predict the fatigue life of AM and wrought NiTi specimens. The specimens fabricated via AM underwent two different heat treatment conditions (*i.e.,* aging followed by air cooling and annealing followed by water quenching). Using the process-dependent parameters, the MSF model could capture the differences in fatigue behavior of each condition. The predicted lower and upper bounds of fatigue life based on the range observed for microstructural features and defect characteristics were able to account for the scatter observed in experimental fatigue data.

Keywords additive manufacturing, cyclic deformation, crack incubation, shape memory alloys, nitinol

1. Introduction

Predictive modeling has proven to be one of the most useful tools that engineers have at their disposal. Through it, engineers can expedite the design process and understand experimental results. Every branch of engineering uses predictive modeling to some degree, and predicting fatigue behavior of metals is critical. Fatigue failure accounts for most of the total failures across all industries annually (Ref 1), so being able to understand and predict fatigue behavior is of paramount importance. The fatigue behavior for materials such as steel and aluminum is well understood and documented; however, this understanding mainly applies to materials formed via conventional manufacturing methods. With the rise of additive manufacturing (AM) processes in the industrial environment, understanding AM processes and their associated changes in material and fatigue properties is important so that the predictive models we have can be adapted and utilized (Ref 2, 3).

One such predictive model is the multistage fatigue (MSF) model. The MSF model, which was originally developed to predict the fatigue damage associated with various microstructural features in cast aluminum alloys (Ref 4), has been adapted and "calibrated" to predict the behavior of a multitude of wrought materials. Because the MSF model admits a wide range of multiscale structures coming from different materials processing methods, it is proposed to capture the fatigue behavior of AM materials (Ref 5). The MSF model defines damage formation and progression in three main stages: fatigue crack incubation (Inc), microstructurally small crack (MSC) growth, and long crack (LC) growth. The MSF model's equations account for all the stages of fatigue damage formation and progression mentioned above, and it is through changing the variables in these equations that the model can be calibrated to a given material.

NiTi (*a.k.a.* nitinol) is known to be the most popular shape memory alloy (SMA). SMAs are exotic materials that show both the shape memory effect (SME), *i.e.,* ability to recover large amounts of seemingly plastic strain upon heating above a critical temperature, and superelasticity (pseudoelasticity), *i.e.,* ability to recover up to sometimes 8% strain upon unloading when above a critical temperature. NiTi has been widely used in both the aerospace and biomedical industries due to its unique mechanical properties, biocompatibility, and resistance to harsh environmental conditions (Ref 6, 7). NiTi (both wrought and AM) is also unique as solution annealing and post-manufacturing heat treatments allow Ni_4Ti_3 and Ni_3Ti precipitate formation, which can change the SMA properties and mechanical behavior of the material (Ref 8–11). However, due to the unique geometries that NiTi alloys are typically required to have, AM processing of NiTi is not only an attractive but

Allen Bagheri and **Yubraj Paudel**, Center for Advanced Vehicular Systems (CAVS), Mississippi State University, Starkville, MS 39762; **Aref Yadollahi**, William B. Burnsed, Jr. Department of Mechanical, Aerospace, and Biomedical Engineering, University of South Alabama, Mobile, AL 36688; and **Mohammad J. Mahtabi**, Department of Mechanical Engineering, University of Tennessee at Chattanooga, Chattanooga, TN 37403; and **Ethan Vance**, Department of Mechanical Engineering, Mississippi State University, Starkville, MS 39762; **Nima Shamsaei**, Department of Mechanical Engineering, Auburn University, Auburn, AL 36849; and **Mark F. Horstemeyer**, School of Engineering, Liberty University, Lynchburg, VA 24515. Contact e-mail: mhorstemeyer@liberty.edu.

Published online: 02 March 2022

sometimes the only alternative to conventional fabrication means.

The laser engineered net shaping (LENS®) process (Ref 12, 13), which is a direct energy deposition (DED) AM technique, consists of injecting powered material into a laser beam created melt pool in a layered fashion. This process allows the microstructural properties of the material to be tailored by changing process parameters such as laser power, scanning speeds, layer thickness, and powder feed rate (Ref 14, 15). Due to the complex physics of AM processes, fabricated materials possess different microstructures, mechanical properties, and fatigue properties when compared with their wrought counterparts (Ref 16). In general, monotonic mechanical properties of AM metallic materials (*e.g.,* tensile and compressive strengths, hardness) are comparable to those of wrought materials. However, microstructural defects, *i.e.,* pores and lack-of-fusion (LOF), which are inherent to the AM process, tend to result in lower fatigue resistance for AM materials when compared with conventionally fabricated ones (Ref 17–19). Lee and Shin (Ref 20) recently quantified the different process–structure relationships upon different heat treatments of AM NiTi, which lays a foundation for the process–structure–property relationships. As mentioned previously the microstructure and mechanical properties can be tailored to be like those of the same wrought materials, but the fatigue resistance is generally lower. Because of this disparity of fatigue behavior, the MSF model must also be calibrated for AM materials alongside wrought materials.

Laser additive manufacturing of NiTi SMAs is currently a topic which attracts significant attention from both academia and industry. Despite the significant efforts devoted to fabrication and processing of AM NiTi SMAs, there are some complex microstructural features occurring due to the laser/material interaction effects that are not fully understood yet (Ref 20, 21). In addition, the correlation between microstructural features and fatigue resistances in the literature regarding AM NiTi is lacking and not well understood (Ref 20, 22). To this regard, having the ability to predict the fatigue behavior based on the AM process-induced microstructural features and defect characteristics would be the first step toward improving the reliability of AM NiTi.

Fatigue performance of a part may not necessarily be dominated by the largest defect but rather a combination of microstructural details, including grain size and level of porosity, defects size, and their location, typically compete together for initiating cracks. Thus, a successful fatigue modeling tool requires not only the abilities to incorporate defect size, but also to link other microstructural details to the fatigue performance. The microstructure-based multistage fatigue (MSF) model, originally created for a cast aluminum alloy (Ref 4), is an appropriate model for such study, since it incorporates a wide range of microstructural details to different stages of fatigue damage, *i.e.,* incubation, microstructurally small crack growth, and long crack growth. The effects of microstructural features (*i.e.,* grain size, mean grain orientation, and misorientation angles) and defect characteristics (*i.e.,* level of porosity, pore size, and their spacing), dictated by the manufacturing and post-manufacturing heat treatment processes, can be directly involved in the fatigue-life prediction. The basis for the MSF was initially founded upon multiscale finite element simulations and only microstructural data were applied toward the end of the development. The incubation stage of the MSF model is based upon a modified Coffin–Manson law. The MSC stage of the MSF model is based upon crack tip displacement (CTD). And the Long Crack (LC) stage is based upon a modified Paris Law. This paper aims to extend the MSF model to predict the fatigue behavior of AM NiTi, subjected to different post-manufacturing heat treatments. The predicted fatigue lives of AM NiTi specimens were compared to their wrought counterparts, and the results are discussed.

2. Material and Experimental Procedures

2.1 Specimen Fabrication and Preparation

The NiTi samples in this work were fabricated via an OPTOMEC LENS® 750 machine retrofitted with 1 kW laser source (Nd:YAG). Gas atomized NiTi powder (100/+325 mesh), based on ASTM standard (Ref 23), was utilized in this study to fabricate the NiTi samples. The powder comprised of 55% nickel and 43% titanium in weight percent (50.7% Ni-48.6%Ti in atomic percent) (Ref 24). Morphology of the powder particles was analyzed via SEM and the majority of the powder possessed a spherical shape. The laser diffraction method was used to measure the sizes of powder particles. The powder sizes ranged from 20 to 200 μm with an average of 66.3 μm and standard deviation of 73.3 μm.

Process parameters, such as laser power, scan speed, and powder flow rate, were tested systematically via trial-and-error, to obtain parts of high dimensional accuracy and minimal porosity. Porosity was investigated by sectioning test cylinders and visually inspecting them using an optical microscope. Final process parameters utilized for fabricating NiTi samples were as follows: laser power of 280 W, scanning speed of 8.47 mm/s, powder feed rate of 0.06 g/s, and layer thickness of 0.5 mm. The LENS® chamber was purged with argon gas to keep the oxygen content below 5 ppm, during the build process.

AM NiTi samples were fabricated in cylindrical rods shape one at a time (single-built), with a diameter of 8 mm and height of 80 mm, vertically on a pure titanium (grade 5) substrate. Archimedes' principle was employed to calculate the density of the fabricated samples. The utilized process parameters resulted in 99.8% of the wrought NiTi density. The cylindrical as-fabricated NiTi samples were machined into dog-bone type specimen for fatigue and tensile tests. The specimens had a uniform gage section of 3.5 mm diameter and 18 mm height, in accordance with ASTM standard for strain-controlled fatigue testing (Ref 25).

Machined specimens were subjected to two different heat treatment conditions: (i) Heat Treatment 1 (HT1): specimens were aged at 550°C for 60 min. followed by air cooling (AC) to room temperature; (ii) Heat Treatment 2 (HT2): specimens were aged at 550°C for 180 min. followed by AC, then, annealing at 550°C for 3 min. followed by water quenching. Both heat treatments were designed to produce a superelastic material at room temperature. The utilized heat treatment procedures for the AM NiTi specimens were obtained based on trial-and-error, in a way that the different plateau stresses were obtained for the two sets of specimens (*i.e.*, AM HT1 and AM HT2) (Ref 23). As such, the fatigue behavior was studied using both the strain–life and stress–life approaches. In order to minimize the effects of surface flaws on the fatigue life, gage sections were mechanically polished using abrasive paper, ranging from a rough level (grit #320) to a smooth level (grit #4000).

2.2 Experimental Procedure

Monotonic tension tests on AM specimens were conducted under strain-controlled conditions at a 0.001/s nominal strain rate until fracture occurred. Cyclic strain-controlled tests were conducted using a servo-hydraulic testing machine at strain ratio of $R_\varepsilon = \varepsilon_{min}/\varepsilon_{max} = 0$ with considering different maximum strain levels (*i.e.*, ε_{max}= 0.6, 0.7, 0.8, 0.9, 1.0, 1.4, and 2.0%). A uniaxial extensometer with a gage length of 15 mm was used for strain measurements. All the cyclic tests were conducted at a constant strain rate (0.01/s). Uniaxial fatigue experiments were conducted in accordance with ASTM E606 (Ref 25) using a sinusoidal loading waveform until failure occurred or 10^6 cycles were achieved, in which the test was considered as "run-out." All experimental tests were conducted at room temperature (~ 24°C).

The microstructural features (*i.e.,* grain size, crystallographic orientation, phase fraction, etc.) and defect characteristics (*i.e.,* porosity, defects size, their spacing, etc.) of samples were examined using a field emission gun scanning electron microscopy (FEG-SEM) equipped with an electron backscatter diffraction (EBSD) detector. Specimens were cut, mounted, and mechanically polished to reveal the cross section area perpendicular to the build direction for microstructural characterizations. Vibratory polishing with colloidal silica suspension was used as a final polishing step before EBSD investigations. Fracture surface of the fatigue specimens was examined using SEM to study the failure mechanisms, including characteristics of crack initiation site and crack progression region.

3. Experimental Results

3.1 Microstructural Characterization

To characterize the microstructure of AM and wrought NiTi, EBSD scans were conducted on the gage sections of fatigue specimens, as shown in Fig. 1(a). Microstructural features—such as grain size, boundary orientation, mean grain orientation, and misorientation—were analyzed to extract microstructural information required for fatigue modeling using MSF model. Like other crystalline materials, microstructural features have a significant influence on the fatigue properties of polycrystalline NiTi alloy. These features (*i.e.,* grain size and grain boundary misorientation) directly affect different stages of fatigue damage, *i.e.,* crack incubation and small crack growth. However, the long crack growth regime is found to be insensitive to microstructural influences. The crack tip displacements are also directly influenced by microstructural properties, affecting the fatigue resistance. For instance, a crack incubated in a region with smaller grains and then propagating into a region of larger grains may require a fewer number of cycles to failure as compared to a crack incubated in a region with larger grains and growing through a region of smaller grains.

McKelvey and Ritchie (Ref 26) were the first to describe the fatigue crack propagation in NiTi material but did not relate any microstructure to the regime. A decrease in grain size increases the fatigue resistance of NiTi alloy (Ref 27). In addition, the fatigue behavior of NiTi depends on the stress concentrations at grain boundaries and precipitate interfaces, which can initiate plastic deformation, thus assisting crack incubation (Ref 21). Grain boundary misorientation for both nanocrystalline (Ref 28) and microcrystalline (Ref 29, 30) also plays a significant role in crack tip propagation through a material. It is worthwhile to mention that although the precipitate formation (i.e., Ni_4Ti_3) is one of the important microstructural factors affecting the fatigue behavior, the MSF model does not explicitly take into account the characteristics of the precipitates. However, the effect of precipitates is implicitly considered in this modeling approach by incorporating the stress–strain response of the material, which is greatly affected by the precipitates.

Figure 1 shows EBSD maps for AM NiTi samples in two heat-treated conditions (*i.e.,* AM HT1 and AM HT2), along with wrought NiTi after being subjected to the same heat treatment as AM HT1. As shown, AM HT1 and AM HT2 (Fig. 1b and c, respectively) specimens exhibit significantly larger grain sizes and aspect ratios as compared with the wrought NiTi specimen (Fig. 1d). Comparing the microstructural features of AM NiTi with wrought NiTi indicates a heterogeneous distribution of grains, with the AM NiTi having a larger average grain size, as can be observed by comparing Fig. 1(b) and (c) with Fig. 1(d). AM HT1 (Fig. 1b) had an average grain size of ~23 μm and AM HT2 (Fig. 1c) had an average grain size of ~17 μm over the cross-sectional area of the gage sections, whereas the wrought NiTi (Fig. 1d) had an average grain size of ~5 μm which is significantly smaller. Because the fabrication process for all AM specimens was the same, the specimens shared a similar microstructure, and hence, the only differences between the grain sizes are a direct result of the different heat treatments. The AM HT1 specimens were quenched via air cooling post-heat treatment, while the AM HT2 specimens were quenched in ice water. Thus, the larger grain size seen in the AM HT1 specimen can be attributed to the slower cooling rate. The annealing process that was performed on AM HT2 appeared to have a significant impact on grain size and distribution.

The EBSD images of AM HT1 and AM HT2 were then filtered to represent the data with a confidence index above 0.1. Figure 2(a) and (b) shows the individual mean grain orientations for AM HT1 and AM HT2, respectively. If necessary, from this the grain misorientation could be calculated to predict a possible crack growth path under a given loading condition. The images were then further filtered to show only the grain boundaries and their misalignments for AM HT1 and AM HT2 (Fig. 2c and d), respectively. In Fig. 2(c) and (d), the grain boundaries are shown for each of the NiTi specimens with the misorientation angle between them represented by the color change from blue (low angle) to red (high angle). As stated previously, the grain boundary misorientation is important for crack tip arrest during crack propagation. The grain boundaries shown in Fig. 2(c) and (d) are separated with at least five-degree misorientation angle.

Figure 2(d) shows that annealing had a greater impact on high-angle-oriented grains, and that the grains tended to grow laterally with respect to the laser beam. Additionally, low-angle-oriented grains with small grain sizes were found in the heat-affected zone (HAZ). The volume fraction of martensitic particles present was 1.2% for AM HT1 specimens, and 2.4% for AM HT2. In general, AM HT2 specimens showed a more homogeneous distribution of martensite particles when compared with AM HT1.

Figure 3(a) and (b) shows the angular pole orientation maps for AM HT1and AM HT2, respectively. The pole figures show relatively higher intensity of (001) and (111) poles away from

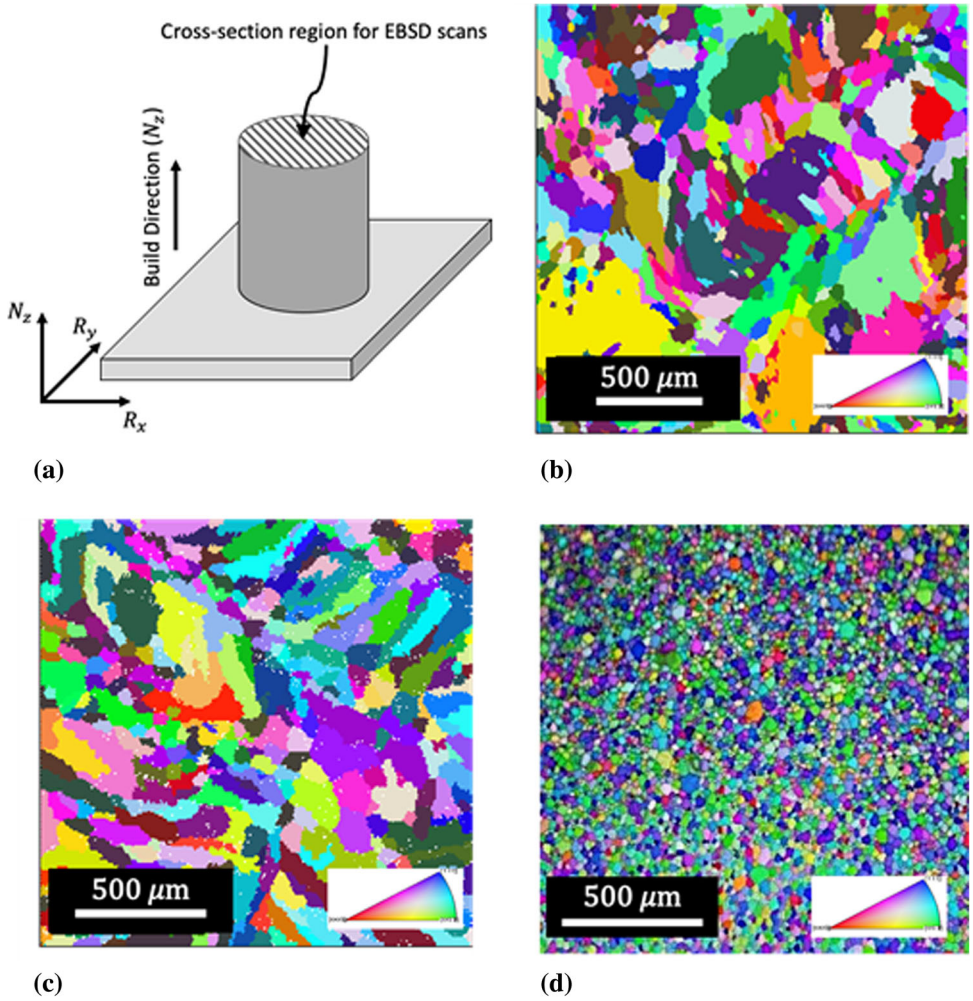

Fig. 1 Electron backscatter diffraction (EBSD) colored map of microstructure from (a) a cross section of NiTi samples in (b) AM HT1, (c) AM HT2, and (d) wrought conditions

the z-direction as compared to (101) plane. However, for the AM HT2 specimens, (001) poles show intensity above two along the x-axis.

EBSD orientation maps of inverse angular poles for AM HT1 and AM HT2 are shown in Fig. 4(a) and (b), respectively. The inverse pole figure in Fig. 4(a) shows that while [101] and [111] fibers spread along the yz-plane for AM HT1, and [001] fiber is preferred along the x-direction. Similarly, in the AM HT2 specimen, the [001] fiber tended to be aligned away from z-direction and [111] fiber aligned toward the z-direction. Previously a relatively strong ⟨111⟩ texture was observed along the rolling/drawing (RD) direction (Ref 31).

The grain mean orientation distribution and the misorientation angle distribution for both AM HT1 and HT2 are shown in Fig. 5(a, b) and (c, d), respectively. As shown, both the grain orientation and misorientation plots are somewhat Gaussian in their distribution. For AM HT1, the average misorientation angle is 33.3 degrees, while it is 31.7 degrees for AM HT2. Due to the similar average misorientation angles between AM HT1 and AM HT2, crack propagation is expected to be similar between the two materials when considering only the applied stresses and grain misorientation.

Table 1 shows the average values for the microstructure properties for AM HT1, AM HT2, and wrought NiTi. As can be observed, AM HT1 had an average grain size that was ~1.3 times greater than those of the AM HT2 specimens. The grain orientation angles as well as the misorientation angles between AM HT1 and HT2 were found to be similar. The values presented in Table 1 as reference values were used to calibrate the MSF model.

In addition to the microstructural features (grain size, boundary orientation, mean grain orientation, misorientation, etc.), defect characteristics (*i.e.,* porosity, defects size, location, and their spacing) play a significant role on fatigue resistance. To this regard, the microstructural samples were examined using a SEM to determine the input values for MSF modeling, including level of porosity (*i.e.,* total void volume fraction), largest void size, and nearest neighbor distance (*NND*) of voids. The volume fraction of porosity was measured via the Archimedes Principle, and the void size and *NND* were garnered directly from the fracture specimens. Defects information needs to be analyzed in a way to be able to distinguish among the situations may occur for AM process-induced defects: highly distributed microporosity (*i.e.,* small spherical pores) with no significant large defects (*i.e.,* large irregular-shape lack-of-fusion regions); presence of large defects; and having large defects near the free surface. For each case, the size and *NND* values were determined appropriately to reflect

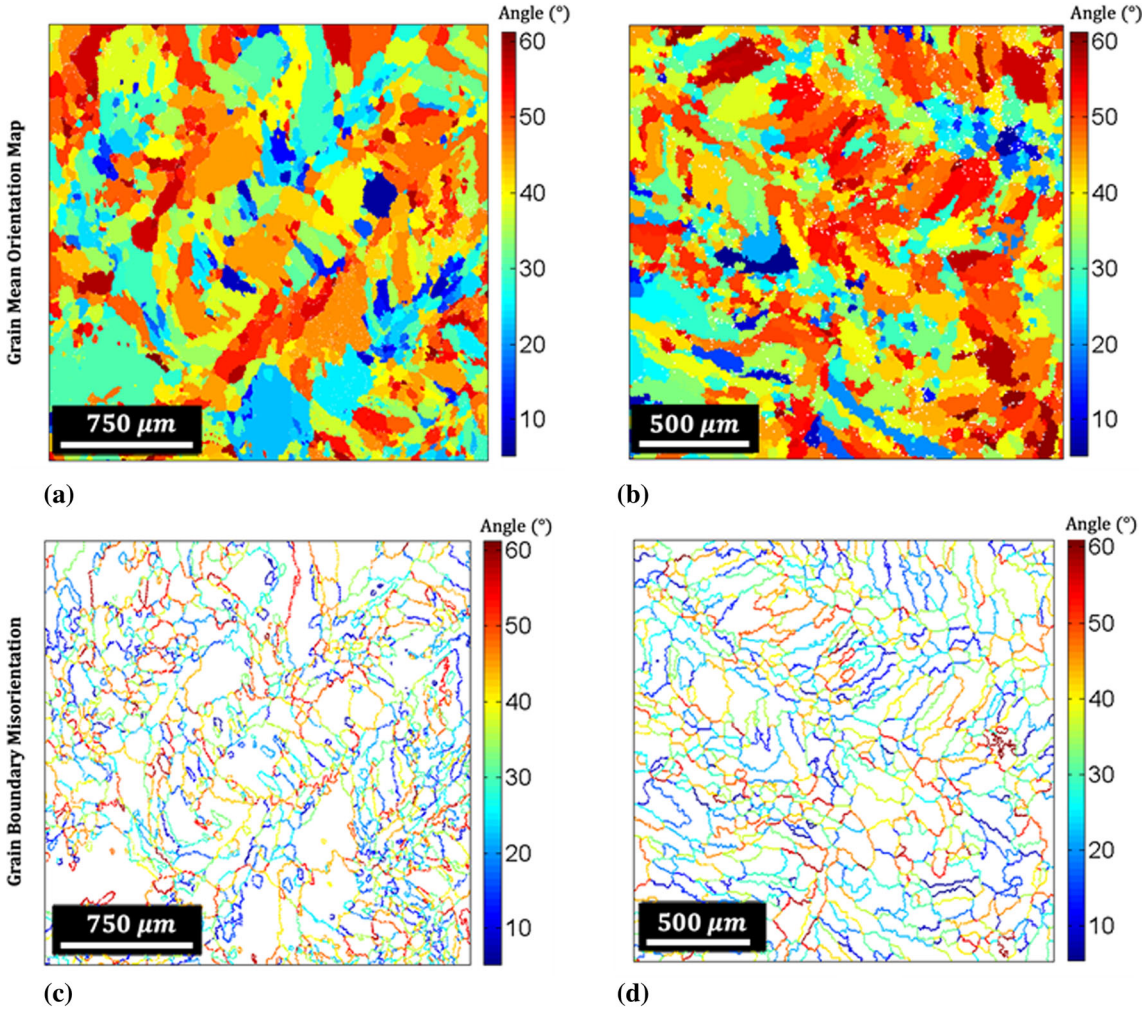

Fig. 2 Electron backscatter diffraction (EBSD) maps with grain mean orientation of (a) AM HT1 and (b) AM HT2. Grain boundary maps of (c) AM HT1 and (d) AM HT2 specimens indicating the grain shape, size, and grain boundary misorientation angles

their effect on the crack incubation and propagation equations. For instance, for the case of having large defects near the free surface, the incubation equation needs to be corrected by the nearest distance of the pore to the free surface, and consequently, the initial crack size in the propagation equations. The analyzed defect characteristics information for AM and wrought NiTi specimens are presented in Table 2. These values were used as the inputs for MSF modeling of NiTi specimens in different conditions (*i.e.,* AM HT1, AM HT2, and wrought).

3.2 Cyclic Deformation

The cyclic stress–strain results showed that increasing number of loading cycles leads to a decrease in the austenite to martensite transformation (A → M) start stress, σ_s^{AM}, of AM NiTi specimens in both conditions (*i.e.,* AM HT1 and AM HT2). In addition, both sets of the AM specimens showed an increase in the stress level corresponding to the maximum strain, *i.e.,* stress range, by increasing number of loading cycles, which indicates the cyclic hardening behavior. However, as reported in other studies on wrought NiTi, after a limited number of cycles (∼150–200 cycles) the stress–strain behavior reaches a stable state (Ref 32–34). Furthermore, the area surrounded by loading and unloading paths, *i.e.,* hysteresis loop, decreased by increasing the number of loading cycles, until the stable state is reached. In the process of generating the cyclic stress–strain behavior for NiTi, different parameters are involved including the stress-induced martensite start stress, σ_s^{AM}, change in the size of the hysteresis loop, and sometimes, accumulation of the residual strain. Furthermore, Mahtabi *et al.* (Ref 32) reported cyclic stress hardening and limited mean stress relaxation for wrought superelastic NiTi. In tests with larger mean strains, where the volume fraction of the martensitic phase is larger, more stress hardening and mean stress relaxation were observed (Ref 35, 36).

For all the AM specimens, the amount of residual strain due to the residual martensitic phase at zero stress was negligible, indicating very stable superelasticity. The midlife cyclic responses of both AM NiTi specimens (*i.e.,* HT1 and HT2) demonstrated a fully superelastic response. For both sets of AM NiTi specimens, the A → M start strain, ε_s^{AM}, appear to be around 1.0%. Midlife cyclic stress–strain response of AM HT1, AM HT2, and wrought specimens are compared in Fig. 6, at the strain amplitude of 1%. As can be observed, the maximum stress level of these three sets of specimens is different. Wrought specimens exhibit slightly lower maximum stress

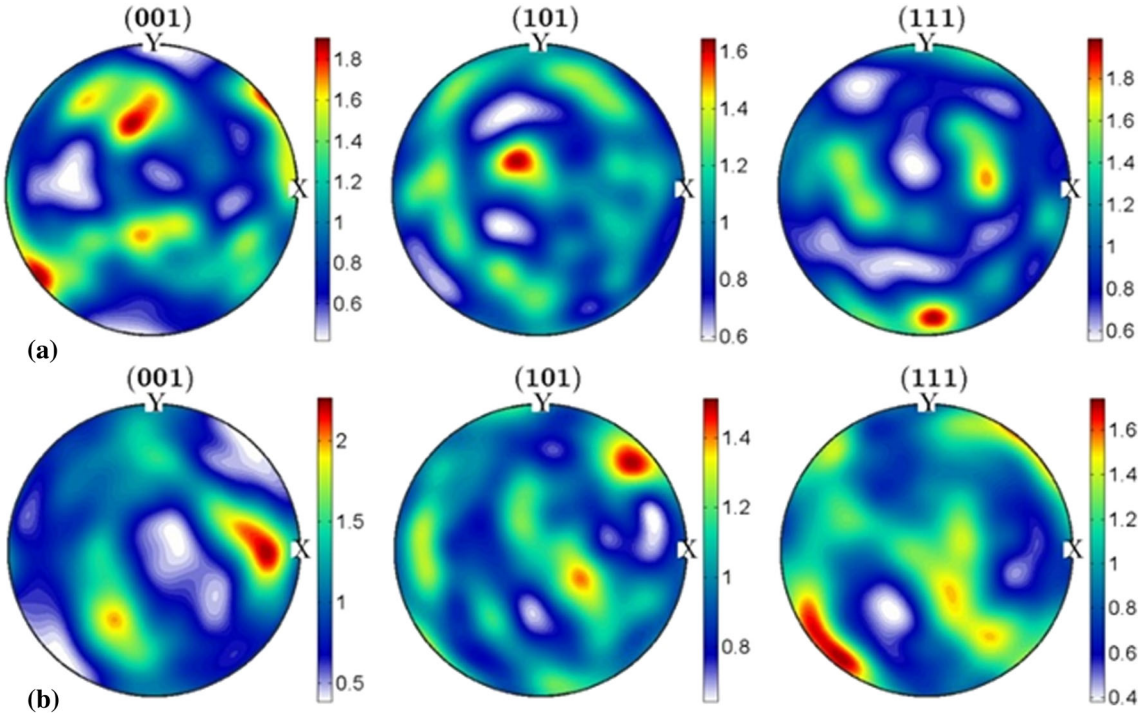

Fig. 3 Pole figures for electron backscatter diffraction (EBSD) maps showing the orientation distribution for (a) AM HT1 and (b) AM HT2 specimens

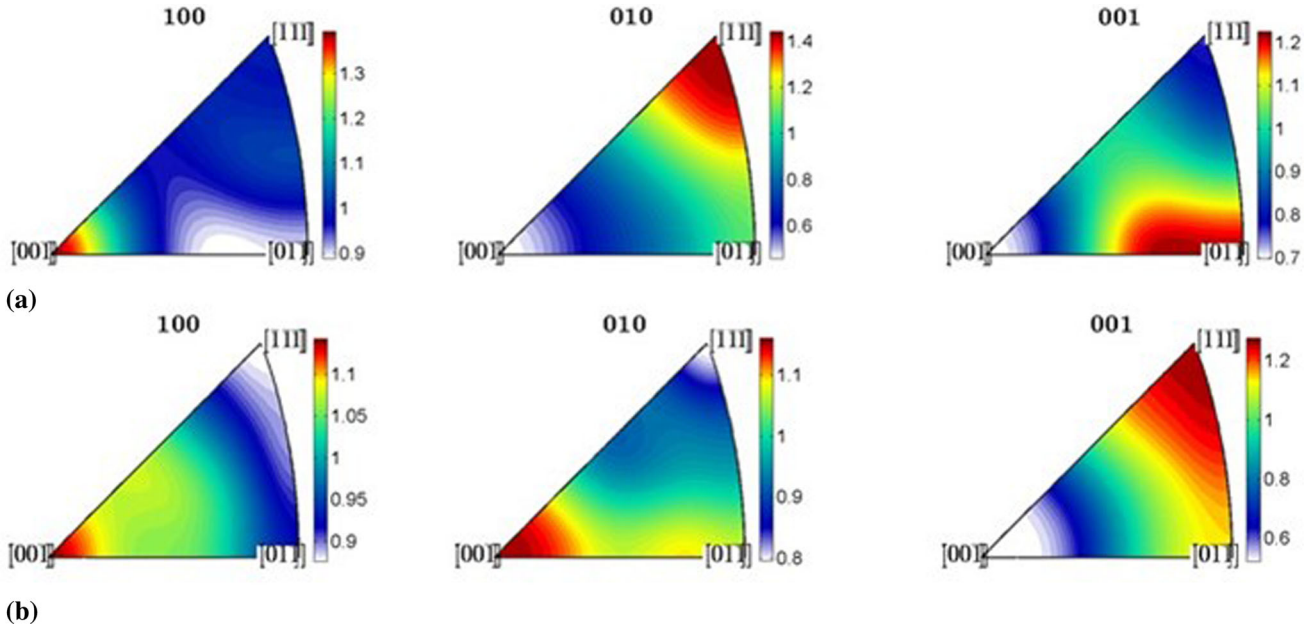

Fig. 4 Inverse pole figures for electron backscatter diffraction (EBSD) maps showing the orientation distribution for (a) AM HT1 and (b) AM HT2 specimens

level than their AM HT1 counterparts, but higher than that of AM HT2 specimens. However, AM HT1 and wrought specimens have similar A → M start stress, σ_s^{AM}, whereas the AM HT2 specimens show a lower level of σ_s^{AM} as compared to their wrought counterpart. These observations indicate that the stress–life and strain–life approaches in fatigue testing and analysis of superelastic NiTi may yield a discrepancy in fatigue behavior (Ref 37).

3.3 Fatigue Behavior

The constant-amplitude pulsating ($R_\varepsilon = 0$) strain-controlled fatigue test results for AM NiTi specimens and their comparison with their wrought NiTi counterparts are presented in Fig. 7. The strain amplitude versus life (ε_a-N) data are shown in Fig. 7(a). The maximum stress versus life (σ_{max}-N) data, based on the midlife stress amplitude of the tests, are also presented in Fig. 7(b). Data points marked by an arrow represent specimens

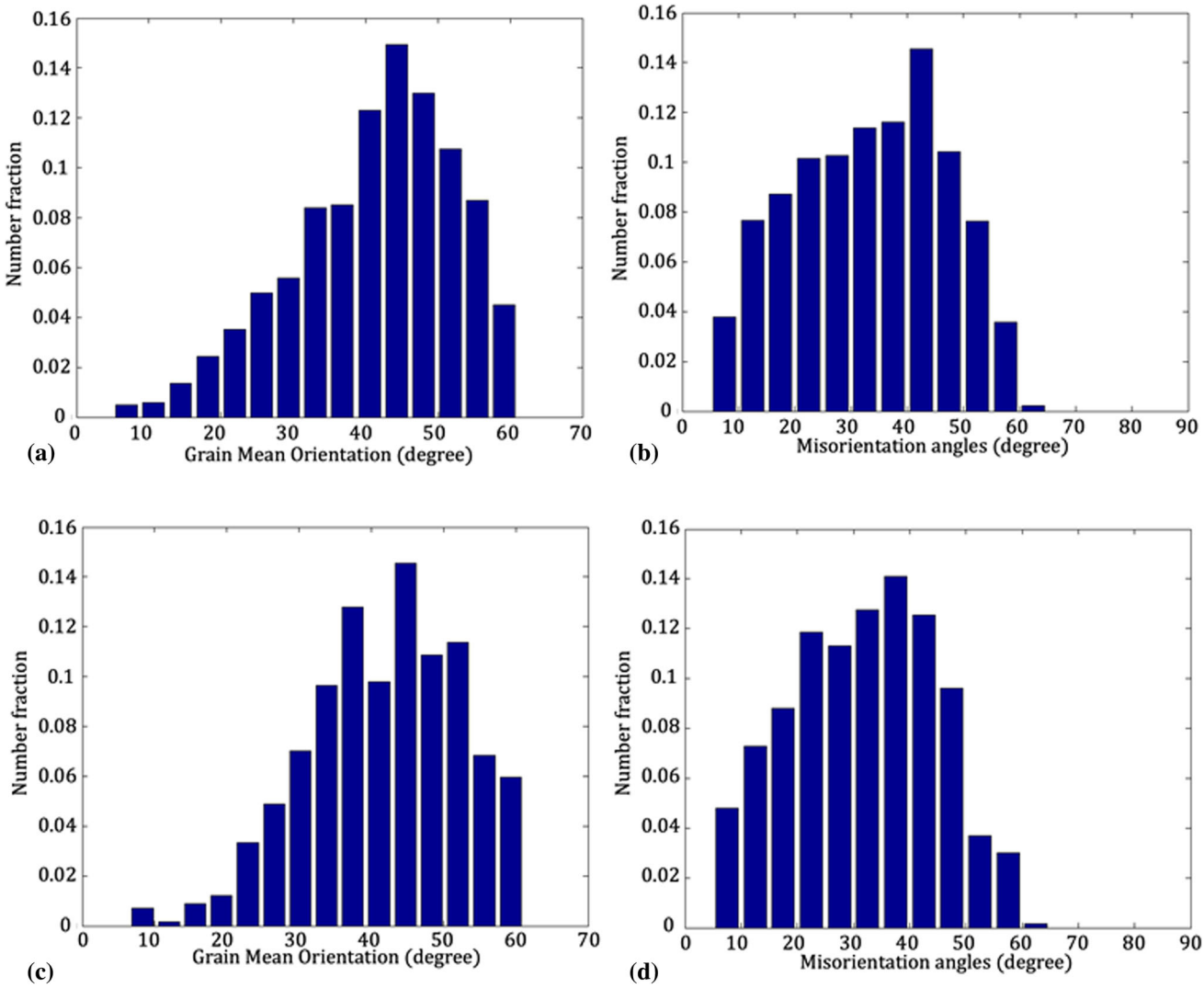

Fig. 5 Comparison of the grain mean orientation distribution (a, c) and misorientation angle (b, d) versus number fraction for AM HT1 and AM HT2 specimens. The fatigue crack growth rate decreases by increasing the misorientation angle due to the increased hindrance to the dislocations emitted by the crack tip along the grain boundaries.

Table 1 Summary of microstructural properties obtained from electron backscatter diffraction (EBSD) of AM and wrought NiTi specimens. Note AM specimens experienced two different heat treatments (HT1 and HT2)

Microstructural properties	AM HT1	AM HT2	Wrought	Reference values
Mean grain size, μm	23 μm	17 μm	5 μm	20 μm
Mean misorientation angle, deg.	33.3	31.7	37.5	32.5
Mean grain orientation angle, deg.	41.2	41.8	46.6	41.5

Table 2 Defect information obtained from AM and wrought NiTi specimens. Note AM specimens experienced two different heat treatments (HT1 and HT2)

Microstructural properties	AM HT1	AM HT2	Wrought	Reference values
Porosity (%)	0.2	0.2	0.01	0.1
Void size (μm)	275	275	25	100
Void *NND* (μm)	150	150	400	200

that failed in the grip, which means that their actual fatigue life was longer than what is reported here.

According to the strain–life plot, shown in Fig. 7(a), the AM HT1 specimens demonstrate comparable fatigue resistance relative to AM HT2 specimens. AM HT2 specimens exhibit slightly longer fatigue lives in the low cycle fatigue (LCF) regime, however, in the high cycle fatigue (HCF) regime, the fatigue lives are very similar. Interestingly, contrary to what was observed for the strain–life behavior, the AM HT1 specimens have noticeably greater fatigue resistance than AM HT2 specimens, in both LCF and HCF regimes, as the stress–life plot shows in Fig. 7(b). This is due to the fact that for a certain strain level in the strain-controlled test, AM HT1 specimens experienced greater stress level (*i.e.,* maximum stress) than their AM HT2 counterparts, as Fig. 6 shows by the cyclic stress–strain plot. Thus, in a strain–life plot the AM HT2 specimens appear to have longer fatigue lives in LCF regime; however, when considering the corresponding maximum stress values, AM HT1 specimens have longer fatigue lives. This indicates that the stress–life and strain–life approaches in fatigue analysis of superelastic NiTi may yield different results. Other studies have also reported the discrepancy in fatigue behavior of superelastic NiTi in stress–life and strain–life approaches (Ref 37). The fatigue resistance of NiTi alloys may have been affected by other influential factors, such as microstructural features (*e.g.*, grain size, grain orientation, *etc.*).

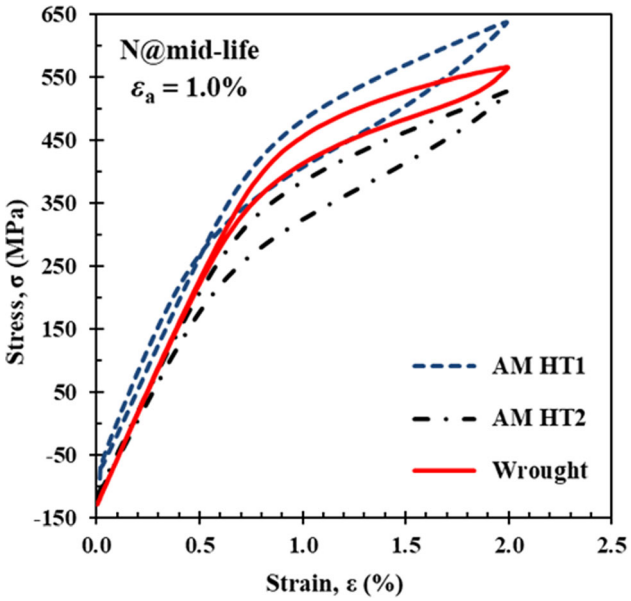

Fig. 6 Comparison of midlife cyclic stress–strain response of AM HT1, AM HT2, and wrought NiTi specimens

Table 3 shows the results of the constant-amplitude pulsating (R_ε = 0) strain-controlled fatigue tests for the NiTi specimens in different conditions, obtained from the stable cycle, measured near the mid-fatigue life of the specimens. As can be observed, the shorter fatigue lives of AM specimens were related to the greater stresses, for the tests at equivalent strain amplitude. For the fatigue tests with strain amplitude below 0.4%, where both heat-treated AM NiTi specimens have similar and linear stress–strain relation, the AM HT1 specimens had higher fatigue resistance. Accordingly, greater fatigue strength can be concluded for AM HT1 specimens as compared to their AM HT2 counterparts.

Comparing strain–life results of AM specimens with previous reports on wrought NiTi (Ref 32, 38), Fig. 7(a) demonstrates that heat-treated AM specimens (*i.e.,* both AM HT1 and AM HT2) have decreased fatigue resistance than wrought NiTi, in both LCF and HCF regimes. However, comparing the fatigue lives in stress–life plot, shown in Fig. 7(b), indicates that AM HT1 can meet the fatigue resistance of its wrought counterpart at LCF regimes. The shorter fatigue life in the midlife and HCF regimes could be related to the microstructural features (*e.g.,* grain size, grain orientation, and formation of precipitates) as well as the presence microstructural defects, such as pores and LOFs.

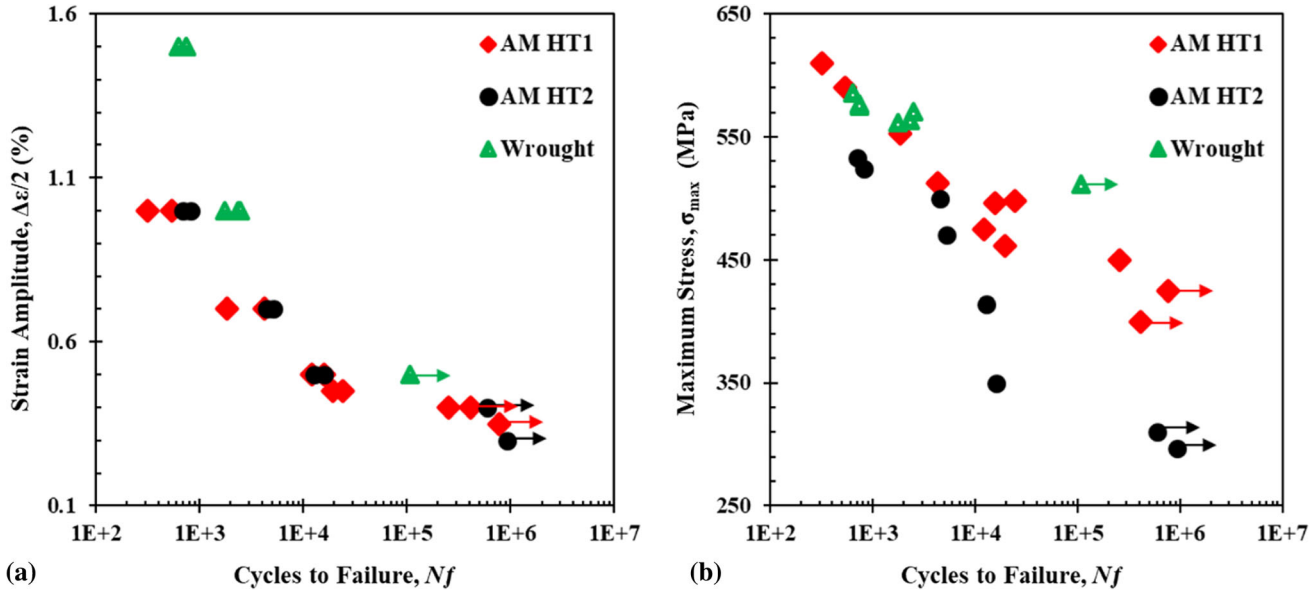

Fig. 7 Comparison of (a) strain–life and (b) stress–life fatigue experimental data of AM NiTi in different conditions (*i.e.,* AM HT1 and AM HT2) with their wrought counterpart

3.4 Failure Mechanisms

Fracture surface of the fatigue specimens was examined using an SEM to investigate the mechanism of failure, including crack initiation sites and crack growth features. Defects with different sizes and shapes were observed on the entire fracture surface area of the AM specimens. As shown in Fig. 8, two common void types were observed on the fracture surface of AM NiTi specimens: (i) pores, resulting from entrapped gas bubbles generated by the laser in the melt pool (in the case of a super-hot melt pool), which are mainly small in size and spherical in shape, shown in Fig. 8(a), and (ii) LOF defects, formed due to low laser penetration depth (in the case of a cold melt pool), which are large and irregular in shape, shown in Fig. 8(b).

Table 3 Summary of constant-amplitude pulsating (R_ε = 0) strain-controlled fatigue test of AM NiTi specimens. Note AM specimens experienced two different heat treatments (HT1 and HT2)

	ε_a (%)	σ_{max} (MPa)	Cycles to failure, N_f
AM HT1	1.0	610	317
	1.0	590	541
	0.7	553	1853
	0.7	512	4254
	0.5	475	12,133
	0.5	496	15,771
	0.45	461	19,461
	0.45	498	24,156
	0.4	450	255,214
	0.4	400	> 407,287
	0.35	425	> 770,710
AM HT2	1.0	533	697
	1.0	524	825
	0.7	500	4465
	0.7	470	5184
	0.5	414	12691
	0.5	350	15,895
	0.4	310	> 601,637
	0.3	297	> 930,673

Fractography of the fractured fatigue specimens revealed that both surface and subsurface defects participated in initiating the cracks. Although specimens were machined and polished to reduce the effect of surface roughness, the remaining defects present in the interior and subsurface area, located near the surface of the specimens, can serve as crack initiation sites. Machining and polishing the specimen's surface brings the subsurface voids to the surface and transforms them into very small surface notches, which induced local stress concentrations causing fatigue damage (Ref 19).

For NiTi alloys, the increase in the stress level due to localized stress concentration around the defects results in the formation of a localized stress-induced martensitic phase. After unloading, the localized stress concentration causes microstructural changes in the area near the defect, including residual martensitic phase, plastic deformation, or a combination of both (Ref 24). Plastic deformation and residual martensite may cause crack initiation in superelastic NiTi due to the sharp interfaces between austenite and martensite phases (Ref 39).

Figure 9(a) and (c) shows the fatigue fracture surfaces of heat-treated AM NiTi specimens (AM HT1 and AM HT2, respectively), tested in the LCF regime (*i.e.,* high strain amplitude). For superelastic NiTi, the majority of total fatigue life was spent in the crack incubation stage and the crack growth contribution was relatively small. However, the fatigue testing regime (*i.e.,* strain/stress amplitude) still influences the crack propagation (Ref 17). A lower strain amplitude (*i.e.,* HCF regime) typically results in a larger crack propagation area, and a greater strain amplitude (*i.e.,* LCF regime) typically results in a smaller crack propagation area. For all the heat-treated AM NiTi specimens, crack propagation zones demonstrated very small size microvoid coalescence fracture mode, as can be observed from Fig. 9(b) and (d). The size of the dimples in AM HT1 specimens, shown in Fig. 9(b), was slightly larger than that of AM HT2, shown in Fig. 9(d), which can be related to the larger grain size of AM HT1 specimens.

The experimental results indicated that in NiTi specimens fracture occurs immediately after the crack incubation stage, perhaps due to high crack growth rates. Thus, the presence of defects, which act as the crack initiation sites, can significantly accelerate the fatigue failure of the AM NiTi.

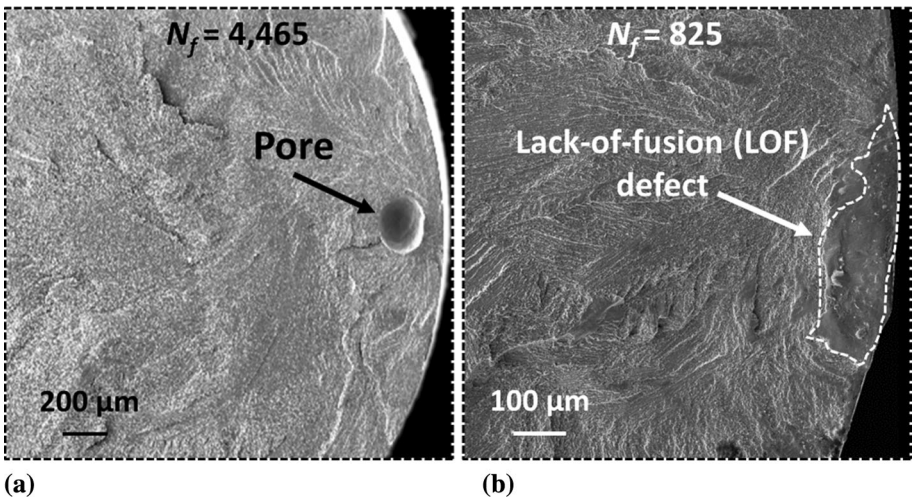

Fig. 8 Scanning electron microscope (SEM) images of fatigue fracture surface showing (a) spherical pore and (b) lack-of-fusion (LOF) defect that served as crack initiation sites

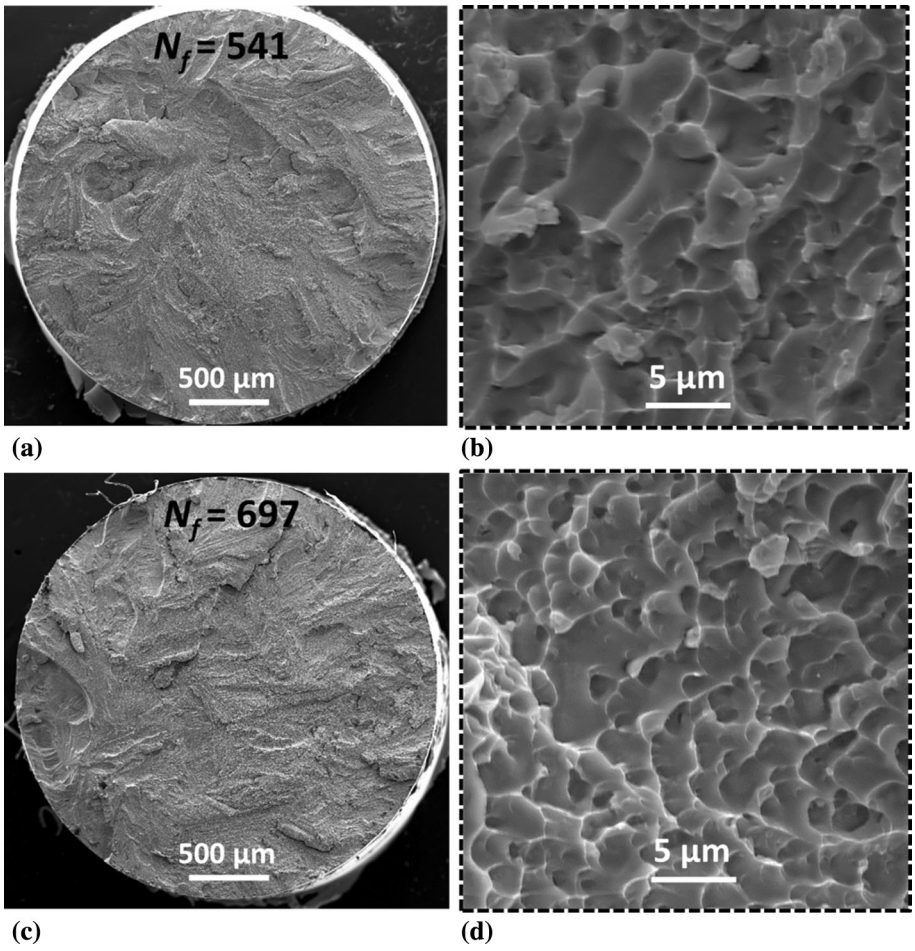

Fig. 9 Overall view of fracture surfaces for heat-treated AM NiTi specimens: (a) AM HT1 and (c) AM HT2, tested in the low cycle fatigue (LCF) regime (*i.e.,* high strain amplitude). High magnification of crack propagation zones shows very small size microvoid coalescence fracture mode for (b) AM HT1 and (d) AM HT2 specimens.

4. Microstructure-Sensitive Multistage Fatigue (MSF) Modeling

4.1 Fatigue Processes in Microstructure

The MSF model is a microstructure-sensitive model that takes into account different stages of fatigue damage evolution, including crack incubation (Inc), microstructurally small cracks (MSC), and long cracks (LC) growth. Detailed information, including the theoretical basis for the model, can be found in (Ref 4). The total fatigue life, N_{Total}, is calculated as the sum of numbers of cycles spent in several consecutive stages as follows:

$$N_{\text{Total}} = N_{\text{Inc}} + N_{\text{MSC}} + N_{\text{LC}} \quad \text{(Eq 1)}$$

where N_{Inc} is the number of cycles to incubate a crack at a micronotch (Ref 4). The two terms "micronotch" and "inclusion" share the same meaning, where the term "inclusion" refers to any microstructural defect present in a material—including second phase particles, intermetallic particles, and pores. The N_{MSC} term refers to the number of cycles needed for a microstructurally small crack (MSC) to propagate; and finally, N_{LC} is the number of cycles needed for a long crack to propagate.

Crack incubation is followed by small crack growth at the micronotch up to about ½ D (D is inclusion size). The small crack growth (MSC) range consists of crack propagation with a crack length ranging from $a_i < a < k \times MS$ where a_i is the initial crack length, MS represents a characteristic length scale of interaction with microstructural (MS) properties, and k is a multiplier between 1 and 3 (Ref 4,40).

The fatigue damage incubation life, N_{Inc}, is calculated by Eq. (2) which is associated with the cyclic damage at the micronotch root. A modified Coffin–Manson law was implemented at the microscale as shown below (Ref 4):

$$C_{\text{Inc}} N_{\text{Inc}}^{\alpha} = \beta = \frac{\Delta\gamma_{\max}^{p^*}}{2} \quad \text{(Eq 2)}$$

where β refers to the nonlocal damage parameter around an inclusion, $(\frac{\Delta\gamma_{max}^{p^*}}{2})$ represents the local average maximum plastic shear strain amplitude, C_{Inc} is the linear coefficient for fatigue crack incubation, and β is its exponential counterpart. The numerical value for exponent α was chosen in a way to fall in the range of the macroscopic Coffin–Mason law. The following relations are used to estimate the numerical value for β:

$$\beta = \frac{\Delta\gamma_{\max}^{p^*}}{2} = Y[\varepsilon_a - \varepsilon_{\text{th}}]^q \frac{l}{D} \leq \eta_{\text{lim}} \quad \text{(Eq 3)}$$

$$\beta = \frac{\Delta\gamma^{p^*}_{\max}}{2} = Y\left(1 + \xi\frac{l}{d}\right)[\varepsilon_a - \varepsilon_{\text{th}}]^q \frac{l}{D} > \eta_{\lim}. \quad \text{(Eq 4)}$$

In Eqs. (3) and (4), ε_a represents the remote applied strain amplitude, and ε_{th} refers to the value for the microplasticity threshold and can be determined by $\varepsilon_{th} = (0.29\sigma_{ult}/E)/(1\text{-}R)$; where E is Young's modulus, σ_{ult} is the ultimate strength, and R is the strain ratio. The ratio of the plastic zone over the inclusion area is subjected to the square root transformation, which is described by the ratio $\frac{l}{D}$. In addition, the micromechanical simulations generate the q and ξ parameters (Ref 40). The limiting ratio, η_{lim}, represents the transition from constrained to unconstrained micronotch root plasticity with regards to the applied strain amplitude (Ref 41). The parameter Y (Ref 4,40) is calculated by the equation $\mathrm{Y} = \mathrm{y}_1 + (1 + \mathrm{R})\mathrm{y}_2$, where R is the stress ratio, and y_1 and y_2 are constant parameters. In the case of completely reversed loading conditions, Y is equal to y_1. Besides, when $(\frac{l}{D})$ hits the limits, some modification is performed on the parameter Y to take into account the geometric effects corresponding to the type of inclusion, the correlation is represented by the equation $\widetilde{Y} = \left(1 + \frac{l}{d}\right)Y$. Therefore, different values for Y might be generated for a debonded particle and a pore of the same size (Ref 42). The equation $(\frac{\Delta\gamma^{p^*}_{max}}{2})$ is used to calculate the correlation of the plastic zone size taking into account the remote strain amplitude.

$$\frac{l}{D} = \eta_{\lim}\frac{\langle\varepsilon_a - \varepsilon_{\text{th}}\rangle}{\varepsilon_{\text{per}} - \varepsilon_{\text{th}}}\frac{l}{D} \le \eta_{\lim} \quad \text{(Eq 5)}$$

$$\frac{l}{D} = 1 - (1 - \eta_{\lim})\left(\frac{\varepsilon_{\text{per}}}{\varepsilon_a}\right)^r \frac{l}{D} > \eta_{\lim}. \quad \text{(Eq 6)}$$

The parameter r is obtained from micromechanical simulations (Ref 42) and refers to the shape constant for the transition to limited plasticity (Ref 43, 44), and ε_{per} is the percolation limit (Ref 4) and is determined by $\varepsilon_{per} = (0.8\sigma_y/E)/(1\text{-}R)$.

The MSC functions were combined into a single mathematical form by McDowell *et al.* (Ref 4). The local driving force for the MSC crack growth is driven by the range of crack tip displacement, ΔCTD, which is proportional to the crack length. Furthermore, in the high cycle fatigue (HCF) regime, the crack growth also depends on the n_{th} power of the applied stress amplitude, $(\sigma_a)^n$, while in low cycle fatigue (LCF) crack growth is correlated with macroscopic plastic shear strain range, $(\frac{\Delta\gamma^{p^*}_{max}}{2})$, which is calculated by the following equations.

$$\left(\frac{da}{dN}\right)_{\text{MSC}} = \chi(\Delta\text{CTD} - \Delta\text{CTD}_{th}) \quad a_i = 0.625D \quad \text{(Eq 7)}$$

$$\Delta\text{CTD} = \mathrm{C}_{II}\left(\frac{\text{GS}}{\text{GS}_0}\right)^{\omega}\left(\frac{\text{GMO}}{\text{GMO}_0}\right)^{\psi}\left[\frac{U\Delta\sigma}{S_{\text{ut}}}\right]^{\xi} a_i + \mathrm{C}_I\left(\frac{\text{GS}}{\text{GS}_0}\right)^{\omega'}\left(\frac{\text{GMO}}{\text{GMO}_0}\right)^{\psi'}\left(\frac{\Delta\gamma^{p^*}_{\max}}{2}\right)^2 \quad \text{(Eq 8)}$$

where χ represents a constant specific value for a given microstructure whose numerical value is typically less than one and is equal to 0.32 for several different alloys (Ref 40). The parameter, a_i, refers to the initial crack length. GS and GS_0 are grain size and reference grain size, respectively. C_I, C_{II}, and ξ are material-dependent parameters that are used to correlate the microstructural effects with the MSC growth (Ref 4,40). The Burgers vector for the matrix is used to set the threshold value for crack tip displacement. The term $\Delta\widehat{\sigma}$ is the combination of the uniaxial effective stress amplitude, $\sigma = \sqrt{\frac{3}{2}\frac{\Delta\sigma_{ij}}{2}\frac{\Delta\sigma_{ij}}{2}}$, and the maximum principal stress ranges, $\Delta\sigma_1$, and is calculated by the relation $\Delta\widehat{\sigma} = 2\theta m\tilde{\sigma}_a + (1-\theta)m\Delta\sigma_1$, with θ falling within $0 \le \theta \le 1$ (Ref 44). Here, θ is a weighting parameter in a way that von Mises stress state has resulted when the $\theta = 1$. The *Schmid* factor, m, falls within $0 \le m \le 0.5$ and accounts for the slip plane and the slip direction of the stressed material and is quantified from the grain orientations. The load ratio effects are considered by employing the parameter U, which is calculated by the equation $U = \frac{1}{1-R}$ (Ref 42). In this study, the ratio of the grain size to the reference size, $\left(\frac{\text{GS}}{\text{GS}_0}\right)^{\omega \text{ or } \omega'}$, was calculated for all AM specimens to investigate the effect of grain size on small crack growth (ω or ω' is a material parameter; GS_0 and GS represent the reference grain size and specific grain size, respectively) (Ref 40). Also, the ratio of the grain misorientation to the reference misorientation, $\left(\frac{\text{GMO}}{\text{GMO}_0}\right)^{\psi \text{ or } \psi'}$, for all specimens was employed to study the correlation between the grain misorientation and small crack growth, where GMO_0 is the reference grain misorientation, GMO is the specific grain misorientation, and ψ or ψ' is a material parameter.

Classical linear elastic fracture mechanics (LEFMs) is applicable to the MSF model for long crack growth stage (Ref 4). However, similar to Jordon *et al.* (Ref 41,43,45), the modeling approach discussed here is centered on the concept of incubation and MSC regimes. Experimental data have validated that MSC can predict fatigue cracks as long as several millimeters (Ref 4).

4.2 Fatigue-Life Prediction

In order to calibrate the MSF model, three categories of input parameters need to be determined: (i) materials fatigue-related data (*i.e.,* incubation, small crack, and large crack constants), (ii) mechanical properties data (*e.g.,* Young's modulus, yield stress, and ultimate tensile strength values), and (iii) microstructural feature and defect characteristic data (*e.g.,* porosity, pore size, pore spacing, grain size, and orientation information). We note that only incubation and microstructurally small crack (MSC) growth regimes were used for fatigue-life predictions, due to relatively small size of the fatigue specimens used in this study. In addition, the long crack growth regime would only constitute a small percentage of the total life in this material. Therefore, MSC laws can be valid on cracks up to several millimeters in length, which is the case for the specimen used in this study. The constants related to the material incubation and MSC growth were obtained and calibrated from wrought NiTi data (Ref 22, 46, 47). The MSF model was first calibrated for one set of strain–life fatigue data as a reference, here AM HT1, based on the mechanical properties and microstructural features (Table 1) and defect characteristic (Table 2) data obtained from experiments. Average monotonic tensile properties of AM and wrought NiTi specimens used in this study are presented in Table 4. The calibrated parameters were used to predict the fatigue life of AM HT2 and wrought NiTi based on the values of mechanical properties (Table 4), microstructural feature data (Table 1) and

defect characteristic information (Table 2) of each set. It should be noted that this modeling approach implicitly takes into account the effect of precipitates (i.e., Ni_4Ti_3) by incorporating the stress–strain response of the material, which is greatly affected by the precipitates. The MSF model predictions for different conditions along with the experimental fatigue-life data are shown in Fig. 10. As seen, the MSF model predictions correlate well with the experimental fatigue data of each set.

Table 4 Average monotonic tensile properties of AM and wrought NiTi specimens. Note AM specimens experienced two different heat treatments (HT1 and HT2).

Mechanical properties	AM HT1	AM HT2	Wrought
Young's modulus, GPa	73	58	73
Yield stress, MPa	580	430	515
Ultimate tensile strength, MPa	900	700	1150

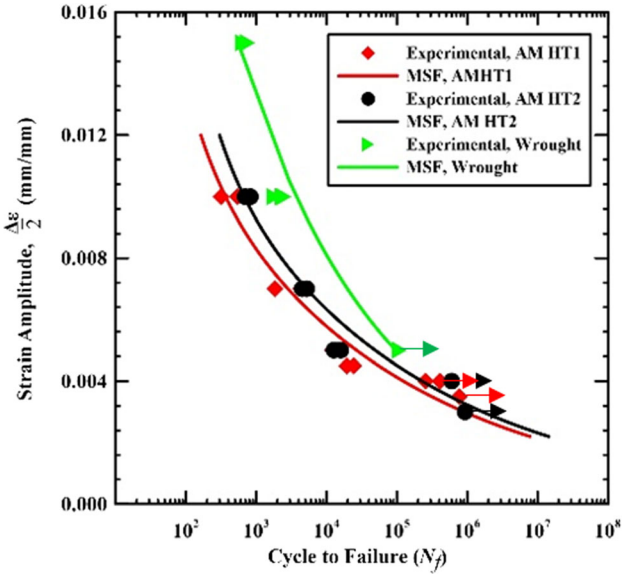

Fig. 10 Multistage fatigue model prediction of strain–life experiment for different conditions

The model constants for material incubation and small crack, used as input for MSF predictions of uniaxial strain–life, are listed in Table 5. These values were kept constant during fatigue-life prediction of these three sets (*i.e.,* AM HT1, AM HT2, and wrought NiTi), and the difference in fatigue behavior has been captured only by changing the processing-dependent parameters of each set (*i.e.,* the values reported in Tables 1, 2, and 4). Since both the AM HT1 and AM HT2 specimens were fabricated together, the defect characteristic data (*i.e.,* porosity, pore size, and *NND*), reported in Table 2, are identical. Thus, the discrepancy in the fatigue behavior of these two groups is related to the differences in post-manufacturing heat treatment procedures, which resulted in distinct microstructural properties (grain size, mean grain orientation, and misorientation angles), and consequently, monotonic tensile properties. As a result, in the MSF modeling, the differences in fatigue life of these two AM groups are captured only by changing the associated mechanical properties, reported in Table 4, and the microstructural data, reported in Table 2. However, for wrought NiTi specimens, differences in both microstructural features and defect characteristics data, arising from manufacturing and post-manufacturing processes, contribute in disparity of fatigue behavior, and thus, implemented in MSF modeling.

Based on the range observed for the microstructural details (*i.e.,* porosity, pore size, distribution, grain size, and orientation) in the experiments, upper and lower bounds can be predicted using MSF model. Figure 11 shows the predicted upper and lower bounds can account for the scatter observed in experimental fatigue data of each set. The uncertainty bands shown in Fig. 11 are calculated using a Monte Carlo method with calibrated parameters as nominal values, and uncertainty of 10% implied in each variable (Ref 48). The uncertainty simulations were conducted for randomly chosen 10,000 datasets within the range of 10% of nominal values.

Table 5 The multistage fatigue (MSF) model parameters used for fatigue-life prediction of AM and wrought NiTi specimens are the same

MSF constant	Value
Material incubation constants	
Constant related to Coffin–Manson law, C_N	0.28
Ductility coefficient in Coffin–Manson law, C_M	0.107
Ductility exponent in Coffin–Manson law, α	0.48
Exponent in remote strain to local plastic shear strain, q	2.9
Constant in remote strain to local plastic shear strain, y_1	3500
Linear constant in remote strain to local plastic shear strain, y_2	0
Geometric factor in micromechanics study, ψ	1.6
Exponent in micromechanics study, r	1.21
Material small crack constants	
Pore effect coefficient, ω	2
Initial crack size contribution, a_{inic}	0.56
Exponent in small crack growth, n	6.93
Low cycle fatigue (LCF) constant in small crack growth, C_I	2.4E+06
High cycle fatigue (HCF) constant in small crack growth, C_{II}	0.2
Final crack size length in small crack growth, a_f	2000

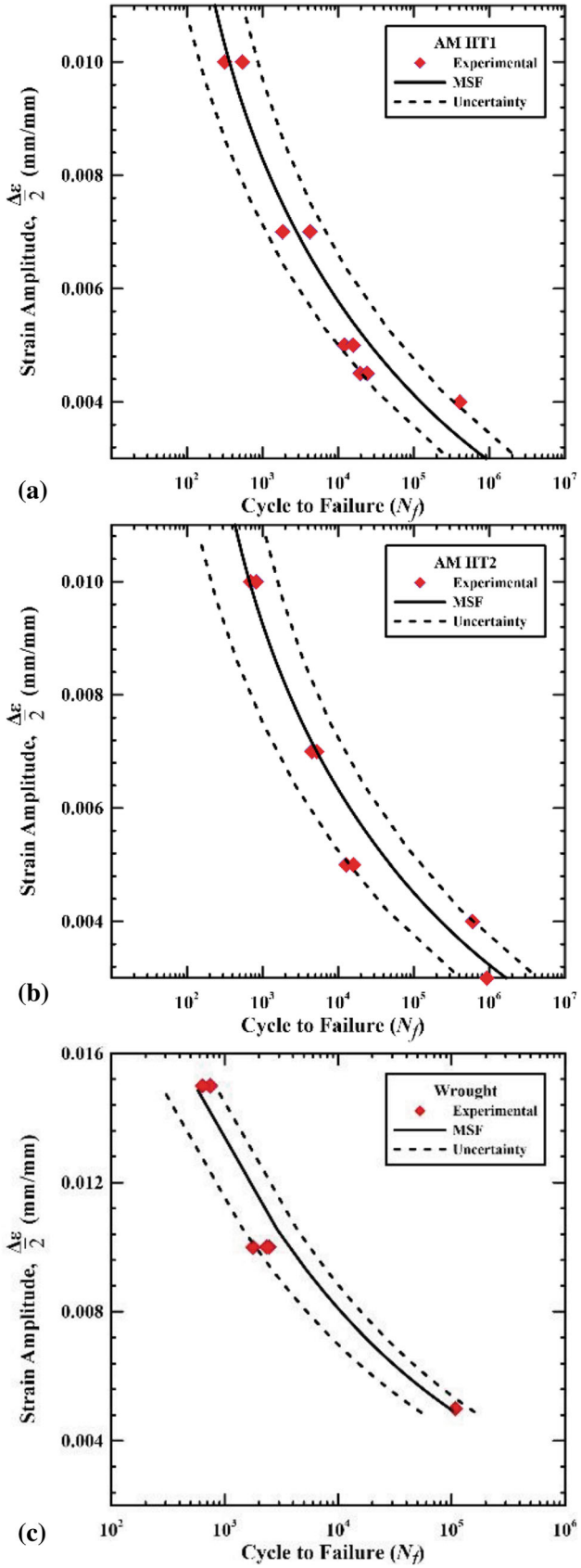

Fig. 11 The predicted upper and lower bounds for (a) AM HT1, (b) AM HT2, and (c) wrought NiTi specimens.

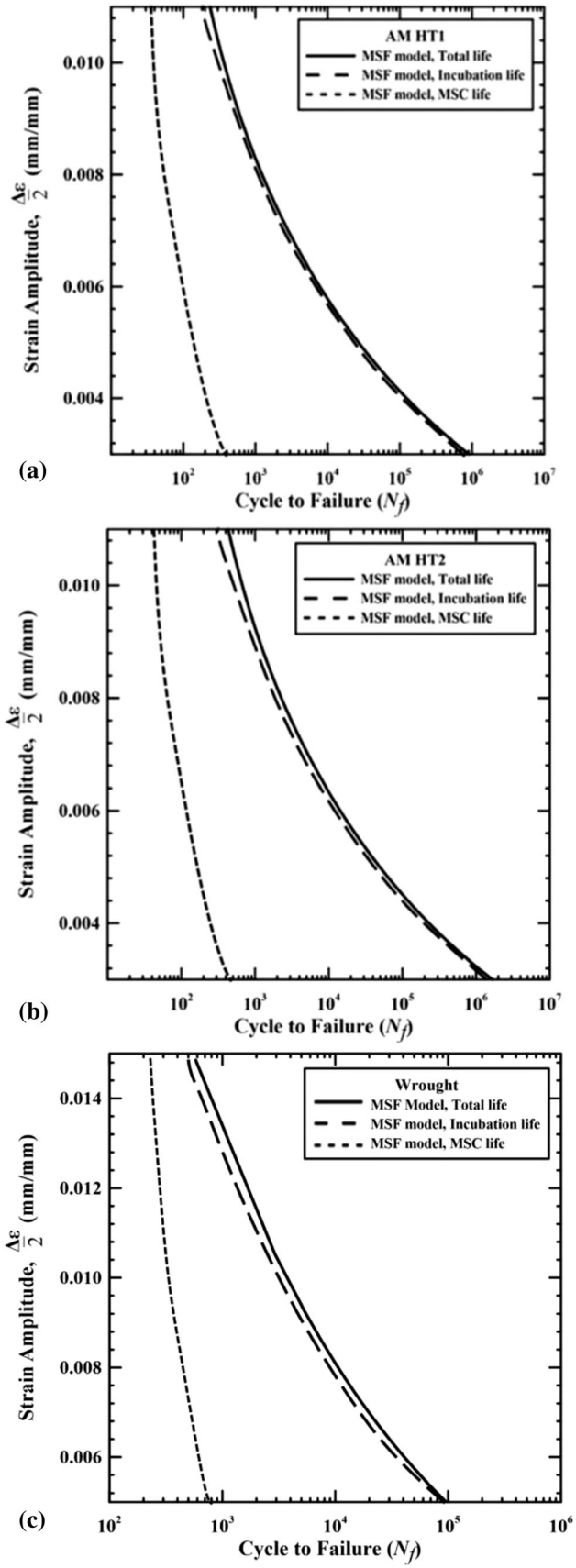

Fig. 12 Multistage fatigue (MSF) model prediction for the breakdown of incubation and small crack growth regimes for (a) AM HT1, (b) AM HT2, and (c) wrought NiTi specimens

In order to explore contributions of the incubation and the MSC growth regimes in the total fatigue life, a breakdown of the fatigue cycles for regime is predicted by MSF model and shown in Fig. 12. The results show that for all the strain ranges, the relative influence of incubation on the total fatigue life is noticeably greater than the MSC growth. In fact, the total fatigue life is dominated by incubation stage. However, as seen from Fig. 12, the MSC growth has more contribution in total fatigue life of all conditions (*i.e.,* AM and wrought NiTi specimens) at lower cycle fatigue regimes. These observations are in agreement with Robertson *et al*. (Ref 22) findings, showing that the fracture of the specimen occurs soon after a crack nucleates and reaches a critical size, which is very small.

5. Conclusions

Microstructure-based multistage fatigue (MSF) model was employed in this study to investigate the process–structure–property relations for cyclic damage and fatigue life of superelastic NiTi fabricated via a direct energy deposition (DED) additive manufacturing (AM) technique. The following conclusions can be drawn based on the experimental and modeling results:

(1) For a certain strain level in the strain-controlled test, AM specimens that underwent aging followed by air cooling (*i.e.,* AM HT1) experienced a greater stress level (*i.e.,* maximum stress) than ones that underwent annealing followed by water quenching (*i.e.,* AM HT2). As a result, a greater fatigue strength was exhibited for AM HT1 specimens when compared to their AM HT2 counterparts.
(2) Due to the presence of AM process-induced defects, pores, and lack-of-fusion (LOF), the AM NiTi specimens showed lower fatigue resistance than their wrought counterparts.
(3) The discrepancy in fatigue life of two AM groups and wrought NiTi specimens was predicted by the MSF model only by using the processing-dependent parameters, associated with each set, *i.e.,* the microstructural features data (grain size, mean grain orientation, and misorientation angles) defect characteristic information (*i.e.,* porosity, pore size, and their spacing).
(4) The MSF model predicted the upper and lower fatigue bounds based on the ranges of the microstructural features and defect characteristics in the experiments, which essentially captures the fatigue scatter observed in experimental data.
(5) Results from MSF modeling indicated that the total fatigue life of the superelastic AM NiTi specimens was dominated by crack incubation in both the LCF and HCF regimes when compared to crack growth.

Acknowledgments

The authors would like to thank the Center for Advanced Vehicular Systems (CAVS) at Mississippi State University for helping support this work.

References

1. R.I. Stephens, A. Fatemi, R.R. Stephens and H.O. Fuchs, *Metal Fatigue in Engineering*, 2nd ed. Wiley, Hoboken, 2000
2. A. Yadollahi, M.J. Mahtabi, A. Khalili, H.R. Doude, and J.C. Newman, Fatigue Life Prediction of Additively Manufactured Material: Effects of Surface Roughness, Defect Size, and Shape, *Fatigue Fract. Eng. Mater. Struct.*, 2018
3. A. Yadollahi, M. Mahmoudi, A. Elwany, H. Doude, L. Bian and J.C. Newman, Fatigue-Life Prediction of Additively Manufactured Material: Effects of Heat Treatment and Build Orientation, *Fatigue Fract. Eng. Mater. Struct.*, 2020, **43**(4), p 831–844.
4. D.L. McDowell, K. Gall, M.F. Horstemeyer and J. Fan, Microstructure-Based Fatigue Modeling of Cast A356–T6 Alloy, *Eng. Fract. Mech.*, 2003, **70**(1), p 49–80.
5. S.H. Seifi, A. Yadollahi, W. Tian, H. Doude, V.H. Hammond and L. Bian, In Situ Nondestructive Fatigue-Life Prediction of Additive Manufactured Parts by Establishing a Process–Defect–Property Relationship, *Advanced Intelligent Systems*, 2021, 2000268
6. T. Duerig, A. Pelton, and D. Stöckel, An Overview of Nitinol Medical Applications, *Mater. Sci. Eng. A*, Elsevier, 1999, **273**, p 149–160
7. A.R. Pelton, J. Dicello, and S. Miyazaki, Optimisation of Processing and Properties of Medical Grade Nitinol Wire, *Minim. Invasive Ther. Allied Technol.*, Taylor & Francis, 2000, **9**(2), p 107–118
8. K. Gall, H. Sehitoglu, Y.I. Chumlyakov, Y.L. Zuev, and I. Karaman, The Role of Coherent Precipitates in Martensitic Transformations in Single Crystal and Polycrystalline Ti-50.8 At% Ni, *Scr. Mater.*, Pergamon, 1998, **39**(6), p 699–705
9. S. Saedi, A.S. Turabi, M.T. Andani, C. Haberland, M. Elahinia, and H. Karaca, Thermomechanical Characterization of Ni-Rich NiTi Fabricated by Selective Laser Melting, *Smart Mater. Struct.*, IOP Publishing, 2016, **25**(3), p 035005
10. M. Nishida, C.M. Wayman, and T. Honma, Precipitation Processes in Near-Equiatomic TiNi Shape Memory Alloys, *Metall. Trans. A*, Springer, 1986, **17**(9), p 1505–1515
11. H.E. Karaca, S.M. Saghaian, G. Ded, H. Tobe, B. Basaran, H.J. Maier, R.D. Noebe, and Y.I. Chumlyakov, Effects of Nanoprecipitation on the Shape Memory and Material Properties of an Ni-Rich NiTiHf High Temperature Shape Memory Alloy, *Acta Mater.*, Elsevier, 2013, **61**(19), p 7422–7431
12. D.M. Keicher and J.E. Smugeresky, The Laser Forming of Metallic Components Using Particulate Materials, 1982, p 51–54
13. C. Atwood, M. Griffith, L. Harwell, E. Schlienger, M. Ensz, J. Smugeresky, T. Romero, D. Greene, and D. Reckaway, Laser Engineered Net Shaping (LENS^{TM}): A Tool for Direct Fabrication of Metal Parts, *International Congress on Applications of Lasers and Electro-Optics*, Laser Institute of America, 1998, p E1–E7
14. A. Bagheri, N. Shamsaei, and S.M. Thompson, Microstructure and Mechanical Properties of Ti-6Al-4V Parts Fabricated by Laser Engineered Net Shaping, *ASME International Mechanical Engineering Congress and Exposition*, American Society of Mechanical Engineers, 2015, p V02AT02A005
15. A. Yadollahi and N. Shamsaei, Additive Manufacturing of Fatigue Resistant Materials: Challenges and Opportunities, *Int. J. Fatigue*, 2017, **98**
16. N. Shamsaei, A. Yadollahi, L. Bian and S.M. Thompson, An Overview of Direct Laser Deposition for Additive Manufacturing; Part II: Mechanical Behavior, Process Parameter Optimization and Control, *Addit. Manuf.*, 2015, **8**, p 12–35.
17. J.T. Sehrt and G. Witt, Dynamic Strength and Fracture Toughness Analysis of Beam Melted Parts, *Proceedings of the 36th International MATADOR Conference*. (Springer, London, 2010), p. 385–388
18. H.A. Stoffregen, K. Butterweck, and Eberhard Abele, Fatigue Analysis in Selective Laser Melting: Review and Investigation of Thin-Walled Actuator Housings, *Solid Freeform Fabrication Symposium*, 2013, p 635–650
19. A. Yadollahi, N. Shamsaei, S.M. Thompson, A. Elwany, and L. Bian, Effects of Building Orientation and Heat Treatment on Fatigue Behavior of Selective Laser Melted 17-4 PH Stainless Steel, *Int. J. Fatigue*, 2017, **94**
20. J. Lee and Y.C. Shin, Effects of Composition and Post Heat Treatment on Shape Memory Characteristics and Mechanical Properties for Laser Direct Deposited Nitinol, *Lasers Manuf. Mater. Process.*, Springer, 2019, **6**(1), p 41–58

21. M.J. Mahtabi, N. Shamsaei and M. Mitchell, Fatigue of Nitinol: The State-of-the-Art and Ongoing Challenges, *J. Mech. Behav. Biomed. Mater.*, 2015, **50**, p 228–254.
22. S.W. Robertson, A.R. Pelton, and R.O. Ritchie, Mechanical Fatigue and Fracture of Nitinol, *Int. Mater. Rev.*, Taylor & Francis, 2012, **57**(1), p 1–37
23. ASTM Standard, B 214-16—Standard Test Method for Sieve Analysis of Metal Powders, 2016
24. A. Bagheri, M.J. Mahtabi and N. Shamsaei, Fatigue Behavior and Cyclic Deformation of Additive Manufactured NiTi, *J. Mech. Behav. Biomed. Mater.*, 2018, **1**(252), p 440–453.
25. ASTM Standard, E 606-12—Standard Practice for Strain-Controlled Fatigue Testing, 2012
26. A.L. McKelvey and R.O. Ritchie, Fatigue-Crack Propagation in Nitinol, a Shape-Memory and Superelastic Endovascular Stent Material, *J. Biomed. Mater. Res. Off. J. Soc. Biomater. Jpn. Soc. Biomater. Aust. Soc. Biomater. Korean Soc. Biomater.*, Wiley Online Library, 1999, **47**(3), p 301–308
27. K.E. Wilkes and P.K. Liaw, The Fatigue Behavior of Shape-Memory Alloys, *Jom*, Springer, 2000, **52**(10), p 45–51
28. P. Zhou, J. Zhou, Z. Ye, X. Hong, H. Huang, and W. Xu, Effect of Grain Size and Misorientation Angle on Fatigue Crack Growth of Nanocrystalline Materials, *Mater. Sci. Eng. A*, Elsevier, 2016, **663**, p 1–7
29. C. Blochwitz, R. Richter, W. Tirschler, and K. Obrtlik, The Effect of Local Textures on Microcrack Propagation in Fatigued Fcc Metals, *Mater. Sci. Eng. A*, Elsevier, 1997, **234**, p 563–566
30. A.S. Azar, L.-E. Svensson, and B. Nyhus, Effect of Crystal Orientation and Texture on Fatigue Crack Evolution in High Strength Steel Welds, *Int. J. Fatigue*, Elsevier, 2015, **77**, p 95–104
31. K. Gall, J. Tyber, G. Wilkesanders, S.W. Robertson, R.O. Ritchie, and H.J. Maier, Effect of Microstructure on the Fatigue of Hot-Rolled and Cold-Drawn NiTi Shape Memory Alloys, *Mater. Sci. Eng. A*, Elsevier, 2008, **486**(1–2), p 389–403
32. M.J. Mahtabi, N. Shamsaei, and B. Rutherford, Mean Strain Effects on the Fatigue Behavior of Superelastic Nitinol Alloys: An Experimental Investigation, *Procedia Eng.*, Elsevier, 2015, **133**, p 646–654
33. K. Gall and H.J. Maier, Cyclic Deformation Mechanisms in Precipitated NiTi Shape Memory Alloys, *Acta Mater.*, Elsevier, 2002, **50**(18), p 4643–4657
34. S. Miyazaki, T. Imai, Y. Igo, and K. Otsuka, Effect of Cyclic Deformation on the Pseudoelasticity Characteristics of Ti-Ni Alloys, *Metall. Trans. A*, Springer, 1986, **17**(1), p 115–120
35. H. El Kadiri, L. Wang, M.F. Horstemeyer, R.S. Yassar, J.T. Berry, S. Felicelli and P.T. Wang, Phase Transformations in Low-Alloy Steel Laser Deposits, *Mater. Sci. Eng. A*, 2008, **494**(1–2), p 10–20.
36. D. Catoor, Z. Ma, and S. Kumar, Cyclic Response and Fatigue Failure of Nitinol Under Tension–Tension Loading, *J. Mater. Res.*, Cambridge University Press, 2019, **34**(20), p 3504–3522
37. M.J. Mahtabi and N. Shamsaei, Fatigue Modeling for Superelastic NiTi Considering Cyclic Deformation and Load Ratio Effects, *Shape Mem. Superelasticity*, Springer, 2017, **3**(3), p 250–263
38. M.J. Mahtabi and N. Shamsaei, A Modified Energy-Based Approach for Fatigue Life Prediction of Superelastic NiTi in Presence of Tensile Mean Strain and Stress, *Int. J. Mech. Sci.*, Elsevier, 2016, **117**, p 321–333
39. R.M. Tabanli, N.K. Simha, and B.T. Berg, Mean Strain Effects on the Fatigue Properties of Superelastic NiTi, *Metall. Mater. Trans. A*, Springer, 2001, **32**(7), p 1866–1869
40. Y. Xue, D.L. McDowell, M.F. Horstemeyer, M.H. Dale and J.B. Jordon, Microstructure-Based Multistage Fatigue Modeling of Aluminum Alloy 7075–T651, *Eng. Fract. Mech.*, 2007, **74**(17), p 2810–2823.
41. J.B. Jordon, M.F. Horstemeyer, N. Yang, J.F. Major, K.A. Gall, J. Fan, and D.L. McDowell, Microstructural Inclusion Influence on Fatigue of a Cast A356 Aluminum Alloy, *Metall. Mater. Trans. A*, Springer, 2010, **41**(2), p 356–363
42. K. Gall, M. Horstemeyer, D.L. McDowell and J. Fan, Finite Element Analysis of the Stress Distributions near Damaged Si Particle Clusters in Cast Al–Si Alloys, *Mech. Mater.*, 2000, **32**(5), p 277–301.
43. D.W. Brown, A. Jain, S.R. Agnew and B. Clausen, Twinning and Detwinning During Cyclic Deformation of Mg Alloy AZ31B, *Mater. Sci. Forum*, 2007, **539–543**, p 3407–3413.
44. D.R. Hayhurst, F.A. Leckie, and D.L. McDowell, Damage Growth under Nonproportional Loading, *Multiaxial fatigue*, ASTM International, 1985
45. L.H. Rettberg, J.B. Jordon, M.F. Horstemeyer and J.W. Jones, Low-Cycle Fatigue Behavior of Die-Cast Mg Alloys AZ91 and AM60, *Metall. Mater. Trans. A*, 2012, **43**(7), p 2260–2274.
46. A.R. Pelton, V. Schroeder, M.R. Mitchell, X.-Y. Gong, M. Barney, and S.W. Robertson, Fatigue and Durability of Nitinol Stents, *J. Mech. Behav. Biomed. Mater.*, Elsevier, 2008, **1**(2), p 153–164
47. A. Runciman, D. Xu, A.R. Pelton, and R.O. Ritchie, An Equivalent Strain/Coffin–Manson Approach to Multiaxial Fatigue and Life Prediction in Superelastic Nitinol Medical Devices, *Biomaterials*, Elsevier, 2011, **32**(22), p 4987–4993
48. J.M. Hughes, M.F. Horstemeyer, R. Carino, N. Sukhija, W.B. Lawrimore, S. Kim, and M.I. Baskes, Hierarchical Bridging between Ab Initio and Atomistic Level Computations: Sensitivity and Uncertainty Analysis for the Modified Embedded-Atom Method (Meam) Potential (Part b), *Jom*, Springer, 2015, **67**(1), p 148–153